Defect trajectories and domain-wall loop dynamics during two-frequency switching in a bistable azimuthal nematic device

A. J. Davidson,[1] C. V. Brown,[2] N. J. Mottram,[1] S. Ladak,[2] and C. R. Evans[2]
[1]*Department of Mathematics and Statistics, University of Strathclyde, 26 Richmond Street, Glasgow G1 1XH, United Kingdom*
[2]*School of Science and Technology, Nottingham Trent University, Clifton Campus, Nottingham, Nottinghamshire NG11 8NS, United Kingdom*
(Received 9 January 2010; published 27 May 2010)

Bistable azimuthal nematic alignment textures have been created in micrometer-scale channels for which one sidewall is smooth and straight and the other possesses a symmetric sawtooth morphology. The optical textures have been observed during dynamic switching between the two stable states in response to dual frequency ac waveform driving of a highly dispersive nematic liquid crystal. The switching processes involves collapsing of filamentlike director reorientation (tilt-wall) loops and the associated motion and annihilation of surface defects along and close to the edge at the sawtooth sidewall. The predictions from both the *n*-director-based Ericksen-Leslie theory and the *Q*-tensor theory are in good agreement with the experimental observations.

DOI: 10.1103/PhysRevE.81.051712 PACS number(s): 61.30.Pq, 42.79.Kr, 61.30.Gd

I. INTRODUCTION

Bistable alignment textures can be produced as a direct result of the interaction between a nematic liquid crystal material and the solid walls that confine the material. To create a technologically useful effect from bistable alignment, for example for display applications, there must be an energy barrier between the physical transformations from one of the stable states to the other stable state, for example via an applied electric field. The two states must also show distinct optical properties, for example dark or light in transmission between crossed polarizers.

Zenithal bistability is where the two stable states differ in the average angle between the nematic *n*-director and the layer normal (the out of plane tilt angle). Zenithal bistable states have been produced by confining a layer of nematic between two parallel plates when there is a difference between the surface anchoring conditions on the two plates [1,2], when one of the plates has a step height change [3], and when at least one of the plates has a one-dimensional surface relief grating pattern [4,5]. The two-dimensional (2D) director configurations of the bistable states for the latter category have been investigated theoretically in the literature by solving the Frank-Oseen continuum theory equations with the aid of conformal mapping [6,7] and finite-element based computational approaches [5,8–10]. The flexoelectrically driven switching between the two stable states has been investigated theoretically in the literature using director-based Ericksen-Leslie approaches [11], *Q*-tensor methods [12] and lattice-Boltzmann schemes [13,14].

Azimuthal bistability is where the average *n*-director orientation for the two stable states occurs at different in-plane twist angles. Azimuthal bistable states have been produced by aligning a nematic layer on a bigrating surface relief structure [15], by fabricating arrays of solid posts in the nematic layer [16], and by confining the nematic in square or polygonal-shaped wells [4,17,18] or in channels with shaped sidewall morphologies [19,20]. It is the latter approach that has been used for the current work where the nematic liquid crystal is confined in a channel that is wide compared to the nematic layer thickness and where one sidewall of the channel is smooth and straight and the other sidewall has a sawtooth morphology. The geometry resembles a "slice through" the zenithal bistable nematic geometry discussed above and in Refs. [4,5]. However, the advantage of the azimuthal geometry used here is that the sidewall can be patterned directly to have any desired morphology on the micrometer scale using straightforward photolithographic processes.

A further advantage from using the sidewall-controlled geometry is that the two-dimensional in-plane nematic *n*-director alignment textures can be directly visualized using standard polarizing microscopy, including the static states [20] and also the time-resolved dynamic switching states during the application of an electric field. A common feature of many of the bistable nematic geometries discussed above is that the occurrence and stability of the different states is critically dependent on the presence of (or otherwise) and the position of nematic defects. The sidewall-controlled geometry in the current work has enabled the visualization of the formation and annihilation of defects and defect trajectories during the switching between bistable states for the first time in this type of geometry. These experimental results have then been directly compared with the predictions of both Ericksen-Leslie theory and *Q*-tensor theory. Dual frequency ac waveform driving of a highly dispersive nematic liquid crystal has been used to produce the bistable switching between the two stable states in this investigation [21–23]. This driving technique has been used because it involves coupling between the applied electric field and the frequency dependent dielectric anisotropy of the nematic liquid crystal, which avoids the complications of ionic migration that are inevitably associated in practice with flexoelectrically driven switching.

II. EXPERIMENTAL INVESTIGATIONS

A. Device geometry and stable states

The structure of the device was manufactured as described in [20] with the geometry as shown in Figs. 1(a) and

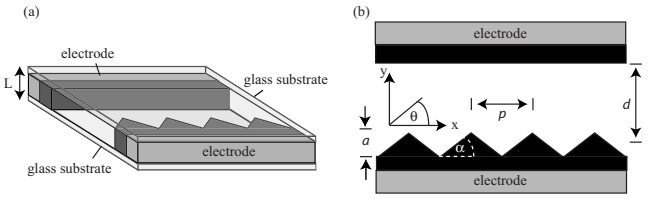

FIG. 1. (a) A 3D representation of the sawtooth cell. (b) A plan section of the sawtooth channel.

1(b) where (a) is a three-dimensional (3D) representation of the device and (b) is the plan section of the device, looking from above. The pitch, p, was fixed at 80 μm with the amplitude, a, of the sawtooth grating fixed at 20 μm, the average distance between the walls was d=90 μm with device thickness L=20 μm. Both the straight and the sawtooth walls were fabricated from SU8 photoresist and they formed open channels in the device along the x-direction. The upper and lower glass substrates were also coated with a thin (0.5 μm) layer of SU8 photoresist so that every surface in the device that was in contact with liquid crystal was fabricated from SU8.

The device was filled with the commercial highly dispersive material nematic liquid crystal, MLC2048 (Merck). This was achieved by heating the material into the isotropic phase and allowing it capillary fill the channels under a vacuum. The two most commonly observed stable states are shown in Figs. 2(a) and 2(b). The states are shown under a magnification of 500× in transmission between crossed polarizers where the input polarizer was parallel to the x axis and the output analyzer was parallel to the y axis. These two states covered the majority of the area of the device and in some areas of the device they coexisted along the same channels separated by distortion "walls." The SU8 coatings on all of the confining surface gave degenerate planar alignment of the nematic liquid crystal MLC2048. The same type of alignment was previously seen in similar structures with the commercial material E7 (Merck) [20]. The two-dimensional director alignment configurations that correspond to these two

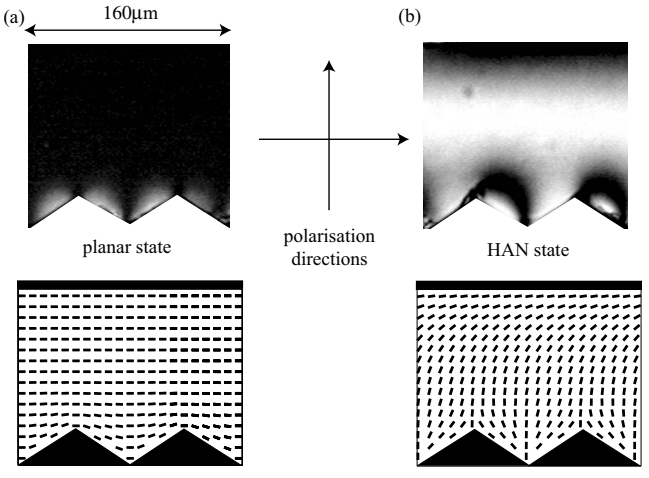

FIG. 2. Two stable states (a) planar and (b) HAN as observed through a microscope with crossed polarisers with corresponding director profiles.

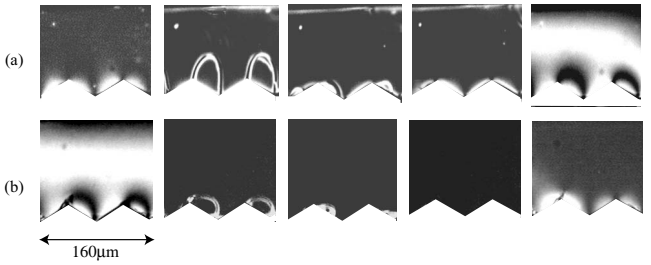

FIG. 3. Switching the cell (a) from the planar state to a HAN state with a low frequency ac field and (b) from a HAN state to the planar state using a high frequency ac field.

stable states are also shown in Figs. 2(a) and 2(b). The stable state shown in Fig. 2(a) will be referred as a *planar* state because the alignment of the nematic n-director in the bulk region remains substantially parallel to the walls of the channel. The stable state shown in Fig. 2(a) will be referred as a *hybrid aligned nematic* (HAN) because the alignment in the region of the sidewall with the symmetrical periodic grating is substantially orthogonal to that sidewall and the director rotates through $\pi/2$ rad in the bulk region of the channel to become parallel to the other straight sidewall. The stability of both of these states is maintained due to the presence of defects near the corners of the sawtooth grating.

B. Switching between states

To produce switching between the two bistable states shown in Figs. 2(a) and 2(b) an in-plane electric field orthogonal to the channels was produced by applying bursts of an ac voltage waveform between the electrodes shown in Fig. 1(a) [21–26]. The electrodes were separated by a distance of 160 μm. The nematic liquid crystal material MLC2048 is highly dispersive, having a positive dielectric anisotropy at low frequencies and a negative dielectric anisotropy at high frequencies with a crossover frequency of 18.5 kHz at room temperature [24]. In Fig. 3(a) switching from the planar state to the HAN state is shown in response to an ac voltage with frequency 1 kHz and 140 V peak. At 1 kHz the nematic responds as a positive dielectric anisotropy material ($\Delta\epsilon$=+3.00), which tends to align the n-director parallel to the direction of the applied field which favors the HAN state in Fig. 2(b). In Fig. 3(b) switching from the HAN state to the planar state is shown in response to an ac voltage with frequency 100 kHz and rms amplitude 100 V. At 100 kHz the nematic responds as a negative dielectric anisotropy material ($\Delta\epsilon$=−2.98), which tends to align the n-director perpendicular to the direction of the applied field which favors the planar state in Fig. 2(a).

There were some slight differences between the switching that was observed in different parts of the channels. The main features of the switching process from the planar state to the HAN state in Fig. 3(a) were: (i) bright filamentlike structures evolved from the peaks and the troughs of the sawtooth sidewall and quickly spanned the width of the channel within a few milliseconds of the field being applied; (ii) nucleated via an instability running through the center of the channel in the x direction the line filaments broke up into

individual loops connected to the sawtooth sidewall; and (iii) the loops slowly shrank and disappeared over a time period of a few seconds. The main features of the switching process from the HAN state to the planar state in Fig. 3(b) were: (i) the brushes connecting each peak to each trough on the sawtooth sidewall became bright filamentlike structures within a few milliseconds of the field being applied; and (iii) the loops slowly shrank and disappeared over a time period of a few seconds. For switching in both directions the shrinking and disappearance of each of the loops was associated with the movement of one or more nematic defects along one facet of each period of the sawtooth sidewall. This part of the switching process will be discussed in detail in the following sections.

III. THEORETICAL MODELS

To better examine and interpret the observed behavior we attempt to simulate the dynamic switching of the device. One possible modeling method for simulating liquid crystal dynamics is the Q-tensor method [27] and significant work has already been done to model defects induced by confined geometries using this method [28,29]. However, in order to model the motion of defects a very accurate numerical mesh is required in the vicinity of regions of high distortion, such as near to a defect core. A single switching simulation can therefore take a large amount of computational time and memory. It would be preferable to find a more efficient method to enable a full examination of the switching behavior. We can achieve this using a director-based Ericksen-Leslie [30] approach as follows.

A. θ model

From observations of the device there is no evidence that the liquid crystal director, $\mathbf{n}$, comes out of the plane or that the upper or lower surfaces have any notable effects on the nematic structure. Therefore we make the assumption that the sawtooth channel shown in Fig. 1 varies in only the lateral two dimensions (x and y) and assume there are negligible top and bottom surface effects. The cell can then be completely modeled in 2D and so there is no need to extend the model to 3D, which would involve a large increase in computer time.

As the director, $\mathbf{n}$, is constrained in the xy plane it is therefore written as

$$\mathbf{n} = [\cos\ \theta(x,y,t), \sin\ \theta(x,y,t), 0], \tag{1}$$

where θ is the angle the director makes with the x axis as shown in Fig. 1(b). We also make the assumption that the electric field, $\mathbf{E}$, is in the y axis so that

$$\mathbf{E} = (0, E_y, 0). \tag{2}$$

To further simplify the equations we assume the field, E_y, is constant throughout the cell. Using these assumptions the total elastic and electrostatic free-energy density for the liquid crystal region is [30],

$$\mathcal{F} = \frac{1}{2}K(\theta_x^2 + \theta_y^2) - \frac{\epsilon_0}{2}E_y^2(\epsilon_\perp + \Delta\epsilon \sin^2\ \theta), \tag{3}$$

where $\theta_x = \partial\theta/\partial x$ and $\theta_y = \partial y/\partial x$ are the spatial derivatives of θ, $\Delta\epsilon = \epsilon_\parallel - \epsilon_\perp$ is the dielectric anisotropy of the liquid crystal, K is the one-constant approximation to the elastic constants [31], ϵ_0 is the permittivity of free space and $\epsilon_\perp$ and $\epsilon_\parallel$ are the electric permittivities perpendicular and parallel to the axis of the liquid crystal director respectively.

On the boundaries we require the liquid crystal to lie parallel to the surfaces. The standard surface free-energy density for this behavior can be written as [31]

$$w_{surf} = W \sin^2(\theta - \alpha), \tag{4}$$

where W is the anchoring strength and α is the angle of the surface with the x axis.

The governing equations for the director are obtained from a balance of the rate of change of the free energy and dissipation taken to be $\mathcal{D} = \gamma_1\dot{\theta}^2/2$, where $\dot{\theta}$ is the time derivative of θ and γ_1 is the rotational viscosity, giving

$$K(\theta_{xx} + \theta_{yy}) - \frac{\epsilon_0}{2}E_y^2\Delta\epsilon \sin(2\theta) = \gamma_1\dot{\theta}. \tag{5}$$

The governing equation for the director at the surface is derived from the balance of surface torques and takes the form

$$-\boldsymbol{\nu}\cdot[K(\theta_x + \theta_y)] = W \sin[2(\alpha - \theta)], \tag{6}$$

where $\boldsymbol{\nu} = [\sin(\alpha), -\cos(\alpha)]$ is the outward unit normal vector at the surface, pointing out from the liquid crystal subdomain.

B. Q-tensor model

To check the validity of this model we have compared results to a Q-tensor model. Again we have used a one-constant approximation for the elastic constants and a constant electric field in the cell as this reduces the computational time and in this system shows little difference when compared to variable field models. The free energy (per unit length in the z-direction) for the Q-tensor is written as [27]

$$F = \int_{\mathcal{A}} (\mathcal{F}_d + \mathcal{F}_t + \mathcal{F}_e)dv + \int_{\mathcal{S}} \mathcal{F}_s ds, \tag{7}$$

where $\mathcal{A}$ is the area of the bulk and $\mathcal{S}$ are the boundary surfaces. The energy density terms are defined as

$$\mathcal{F}_d = \sum_{\substack{i=1,2,3 \\ j=1,2,3 \\ k=1,2,3}} \frac{K}{4S^2}\left(\frac{\partial Q_{ij}}{\partial x_k}\right)^2, \tag{8}$$

$$\mathcal{F}_t = a\ \mathrm{tr}(\mathbf{Q}^2) + \frac{2b}{3}\mathrm{tr}(\mathbf{Q}^3) + c[\mathrm{tr}(\mathbf{Q}^4)], \tag{9}$$

$$\mathcal{F}_e = -\frac{1}{2}\epsilon_0\epsilon E_y^2, \tag{10}$$

$$\mathcal{F}_s = \frac{W_s}{2}(\mathbf{Q} - \mathbf{Q_s})^2, \tag{11}$$

where S is the bulk order parameter [27], $\boldsymbol{\epsilon}$ is the dielectric tensor, a, b, and c are thermotropic coefficients, W_s is the Q-tensor anchoring strength linked to the θ-model anchoring strength, W, in Eq. (4) by the relationship $W_s = W/(2S^2)$ and the symmetric traceless tensor $\mathbf{Q}$ is defined as

$$\mathbf{Q} = \begin{pmatrix} q_1 & q_2 & q_3 \\ q_2 & q_4 & q_5 \\ q_3 & q_5 & -q_1 - q_4 \end{pmatrix}, \tag{12}$$

where $\mathbf{Q_s}$ is the preferred tensor on the boundary taken to be equivalent to a uniaxial director parallel to the surface with $S = S_{eq}$. If the liquid crystal is uniaxial with a director $\mathbf{n}$ as defined in Eq. (1) we can associate the components of $\mathbf{Q}$ with the director angle thus,

$$q_1 = S\cos^2\theta - \frac{1}{3}S, \quad q_2 = S\sin\theta\cos\theta, \quad q_3 = 0,$$

$$q_4 = S\sin^2\theta - \frac{1}{3}S \quad \text{and} \quad q_5 = 0. \tag{13}$$

The governing equations for this model are derived in a similar way to the θ-model using a dissipation term $\mathcal{D} = [\gamma_1/(4S^2)]\mathrm{tr}(\dot{\mathbf{Q}}^2)$. We can recover the director angle $\theta(x,y,t)$ by finding the largest eigenvector of the Q-tensor at each point in the liquid crystal.

C. Numerical solution method

In both cases (θ-model and Q-tensor model) the governing equations can be solved using a finite-element package [32] to determine the resulting director profile for a given geometry. As there is only one variable to calculate with the θ-model the solution is reached much faster than the Q-tensor, which used five variables. Using the same mesh size with the same parameters, the Q-tensor model took over 14 times longer to reach the same solution as the θ-model. The elastic and dielectric properties of the liquid crystal are approximated in the simulations as $K = 1.75 \times 10^{-11}$ N and $\Delta\epsilon = \pm 3$. All other variables in the simulations were approximations based on other liquid crystal materials: $\gamma_1 = 0.175$ N m^{-2} s^{-1}, $W = 1.75 \times 10^{-5}$ N m^{-1}, $a = -0.112 \times 10^4$ N m^{-2}, $b = -0.64 \times 10^4$ N m^{-2}, and $c = 1 \times 10^4$ N m^{-2}. Here the values of a, b and c are approximately two orders of magnitude less than those measured experimentally [27]. This increases the natural length scale of variations in the order parameter and increases the overall defect size, resulting in a faster numerical solution of the problem while still providing accurate results [12]. We also note the anchoring strength, W, relates to relatively strong anchoring as, without a large anchoring strength the device cannot support multiple stable states. The permittivity of free space is $\epsilon_0 = 8.85 \times 10^{-12}$ C^2 N^{-1} m^{-2} and the constant field is defined as $E_y = V/d$, where V is the potential difference between electrodes, taken to be 140 V and $d = 160$ μm is the distance between the electrodes.

One disadvantage of the θ-model is that it does not allow the correct representation of defects moving in the bulk of the cell [33]. However, in the case of the sawtooth grating modeled here, where the anchoring is relatively weak, it appears that any defects created stay close to the surfaces and so this method still provides reliable results.

D. Transmission calculation for crossed polarizers

To compare the theoretical results to those observed experimentally through crossed polarizers it would be helpful to produce optical transmission images from the model of the device. To do this we use the equation [34].

$$T = \sin^2[2(\chi + \theta)]\sin^2\left(\frac{\delta}{2}\right), \tag{14}$$

where T is the optical transmission, χ is the angle of rotation of one of the crossed polarisers from the x-axis (taken here to be $\chi = 0$) and δ is the retardation of the liquid crystal layer defined as

$$\delta = \frac{2\pi n_\perp}{\lambda}\left(\frac{n_\perp}{n_\parallel} - 1\right), \tag{15}$$

with the wavelength of light taken to be $\lambda = 600$ nm, and the extraordinary and ordinary refractive indices of the liquid crystal taken to be $n_\parallel = 1.721$ and $n_\perp = 1.5$, respectively. With these values T can have a value between 0 (represented as black in the following figures) and 1 (represented as white).

IV. MODELING COMPARISON: SWITCHING PLANAR TO HAN

Using the model described above we can produce a director profile of the planar state using $\theta = 0$ as an initial condition. With a positive dielectric anisotropy, $\Delta\epsilon = 3$, and an applied voltage of $V = 140$ V the θ-model was used to simulate the switching from the planar state to the HAN state. Figure 4 shows a comparison between the experiments and the θ-model. Using Eq. (14) the transmission for the simulation is shown, and compares well with the experimental results. When the voltage is applied the liquid crystal director rotates toward a vertical orientation due to the dielectric response with the electric field. The formation of the large director reorientation loop occurs as soon as the field is applied and, as the field is maintained, the loop reduces in size until it disappears. When the voltage is then removed the cell relaxes into the HAN state. To check the accuracy of the θ-model we compared our results with that produced by the Q-tensor model and as can be seen there is a very good comparison between the two methods.

The loop itself is created due to a frustration in the director profile between different parts of the sawtooth grating, with the director rotating in different directions, $\theta \to \pi/2$ and $\theta \to -\pi/2$, to align with the field, as shown in Fig. 5(a). Between these two regions the director profile is held at $\theta = 0$ and is unable to rotate to align with the field unless the symmetry of the system is broken. In an experimental device, flow effects and small manufacturing inaccuracies result in the symmetry being broken and one state being pref-

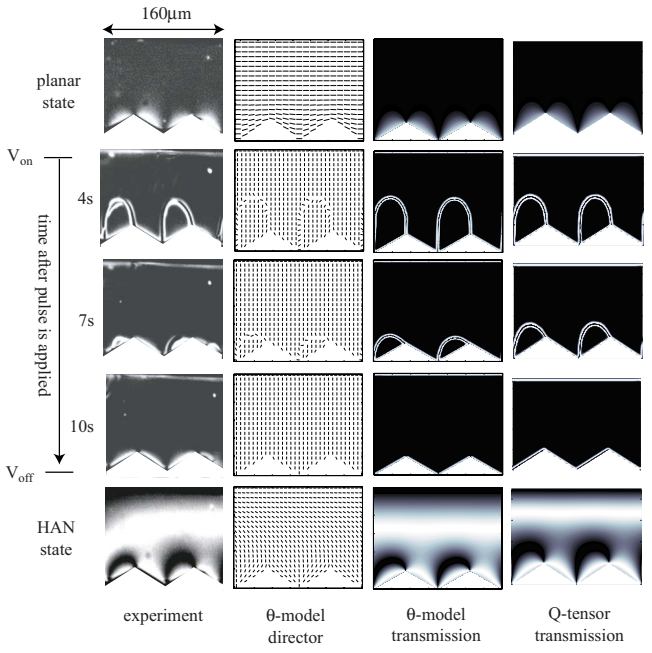

FIG. 4. (Color online) Comparison of experimental results of switching the cell from the planar state to the HAN state with the computed θ-model director profile, the associated transmission image and the transmission calculated from the Q-tensor model.

erable to the other. In this situation the liquid crystal material near the upper surface tends toward one of these two rotations. In our model there is no preference to either state on the upper surface and so when a voltage is applied the result can be seen in Fig. 5(b). To simulate the asymmetry as seen in the experimental device we have introduced in our model a small pretilt of 0.01 radians on the upper surface which makes one orientation (in this case the $\theta=-\pi/2$ state) more preferable. This can be seen in Fig. 5(c).

As the loop decreases in size the ends of the loop eventually begin to move together along the surface of the grating until the loop disappears, as shown in Fig. 6. Figure 7 shows how the x coordinate of the loop edges A and B move together as a function of time. The dashed line in Fig. 7(a) represents experimental data. As can be seen from the experimental and theoretical data the loops start to shrink at around the same time, a few seconds after the voltage pulse is applied, and both disappear around the same time, approxi-

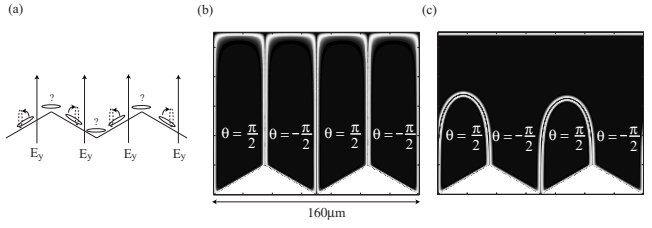

FIG. 5. (a) The direction of rotation for the liquid crystal molecules near the surface depends on the surface orientation. (b) 0.1 s after the voltage is applied when the upper surface has no pretilt. (c) 0.1 s after the voltage is applied when the upper surface has a small pretilt of 0.01 radians, preferring the $\theta=-\pi/2$ state.

FIG. 6. The loop shrinks until it disappears near the middle of a grating edge.

mately 9 s afterward. When looking at how the volume of the loop changes with respect to time it can be seen that it decreases linearly [as shown in Fig. 7(b)] from the moment the pulse is applied. We note here that the experimental results match closely with the numerical results. When the loop is formed after the pulse is applied it smoothly reduces in height but the curvature of the top of the loop does not change until most of the loop has already disappeared, after which the ends of the loop begin to move together. Examining the elastic energy of the cell, from the θ-model, we can see that after the voltage is applied the energy decreases, at first linearly but later, as the defects start to move, in a nonlinear fashion, reaching a constant value after the loop has disappeared (at approximately 10 s). The energy further decreases when the voltage is removed and the cell relaxes into the HAN state.

From Fig. 8(a) we can see that, due to the sharp edges of the sawtooth structure, there are two reorientation points or "surface defects" at P_1 and P_2. The strength of these defects are measured as the angle of rotation of the director moving around the defect in an anticlockwise direction. From this we see the director rotates through angles of -2α and 2α radians at P_1 and P_2. Due to the sharp nature of these points there will always be a pinned defect at both P_1 and P_2. When the voltage is applied a loop appears, consisting of a region of high-director distortion where the director rotates through π radians (from $\pi/2$ to $-\pi/2$). The energy of the system is proportional to the length of the loop, where the distortion if focused. Therefore, the smaller the loop becomes the lower the overall energy of the cell is as seen in Fig. 7(c). The loop itself is forced to decrease by the dominant bulk elastic forces in the cell. Shortly after the pulse is applied and the loop has decreased in size, the ends A and B start to move toward each other [as shown in Fig. 8(b)]. The defect pinned at P_1 remains unchanged as a -2α defect but P_2 has is transformed into a $(-\pi+2\alpha)$ defect. The points A and B indicate where the loop meets the surface. On the surface at point A the director has no defect whereas on the surface at point B there is a π defect. This defect at point B is always more likely to form near the top of the grating as there is less confinement than on the bottom of the grating and the energy can dissipate more easily.

After points A and B meet the π defect at $A+B$ begins to move toward P_1 as shown in Fig. 8(c). Once $A+B$ arrives at P_1 the defects merge and become a $\pi-2\alpha$ defect as can be seen in Fig. 8(d).

Features in longer channels

When looking at switching from the planar to the HAN state in a long channel, both HAN states were observed

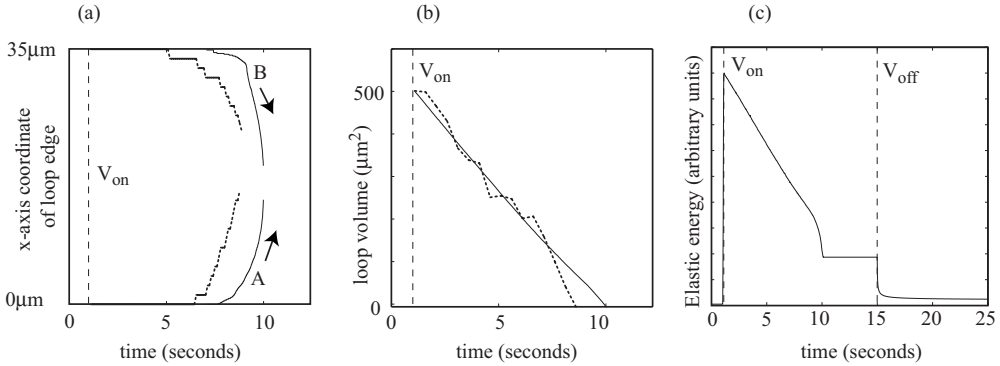

FIG. 7. (a) The x-coordinate of the loop edges versus time for experimental data (dashed line) and numerical results (solid line). (b) The volume of the loop decreases linearly after the voltage is applied for experimental data (dashed line) and numerical results (solid line). (c) The elastic energy of the system decreases while the voltage is on until it reaches a constant value, then decreases as the cell relaxes into the HAN state.

forming in the experimental device. As mentioned previously, there is usually some small manufacturing inaccuracies which result in the symmetry being broken and one HAN being more preferable to the other. In a long channel there may be many such inaccuracies, which can result in some areas switching to one HAN state while different areas switch to the other HAN state. In each of these states the director is rotated in a different direction and so between two such HAN states there is a thin filament region reaching from the lower surface to the upper surface where the director rotates through π radians, similar to the loop show earlier (see Fig. 9). The nature of this line depends on the elastic energies of the two adjacent HAN states, with the line bending in the direction of the HAN state with the lower elastic energy.

To model this type of occurrence we changed the pretilt on the upper surface such that it had an energy minima when $\theta=0.01\sin(P_x\pi/70)$ where P_x is the distance along the upper surface in microns from a position directly above a sawtooth trough. This means that in the first pitch of the sawtooth grating (which is 80 μm long) the upper surface favors a small positive angle of θ and in the next pitch it favors a small negative value of θ, producing different HAN states, respectively. As seen in Fig. 9 the model compares well with the experimental observations of this line. It can also be seen that when the voltage is removed the area around where the line appeared does not switch into either of the HAN states and so for more reliable switching it is necessary to force one HAN state to be predictably more energetically favorable than the other. This can be done by changing the symmetry of the sawtooth grating, the extent of which is currently under investigation.

V. MODELING COMPARISON: SWITCHING HAN TO PLANAR

As discussed previously, the reverse switching, from HAN to planar state, is achieved experimentally by applying a voltage at a sufficiently high frequency to cause the dielectric anisotropy of the liquid crystal material to become negative. In the θ-model we can model this behavior by simply changing the sign of the dielectric anisotropy (in this case set to $\Delta\epsilon=-3$ corresponding to a high-frequency ac field). As can be seen from Fig. 10 the theoretical results and the transmission results produced from the θ-model again compare well with both the experimental results and those produced

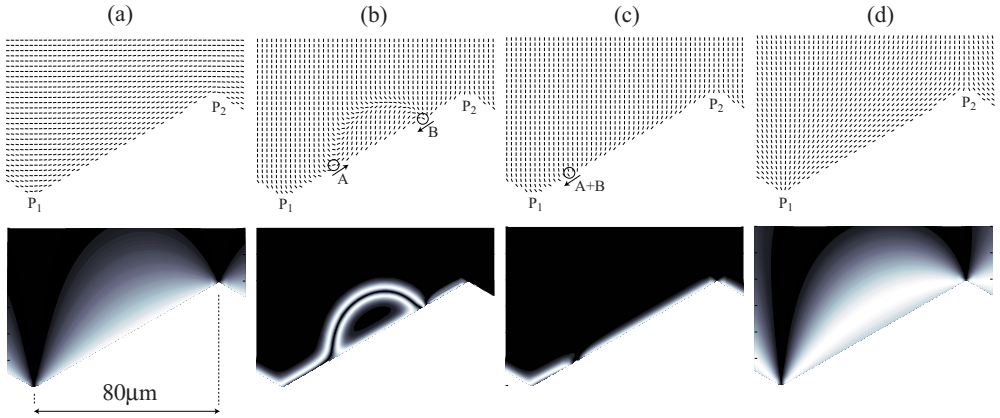

FIG. 8. (Color online) Enlarged plot of the director and corresponding transmission plots when switching from the planar state to the HAN state. (a) Before the pulse is applied. (b) After the pulse is applied and the loop has decreased in size. (c) After the loop has disappeared. (d) The final state after the pulse is removed.

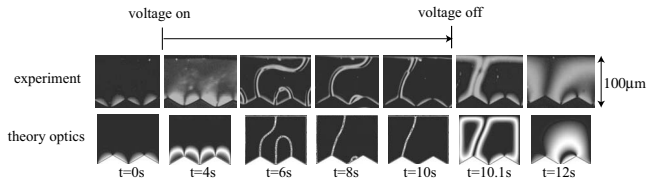

FIG. 9. When a voltage is applied across a long channel a thin line of high distortion can appear connecting the upper and lower surfaces.

by the more accurate Q-tensor model. One notable difference is that in the Q-tensor results the defects can be seen leaving the surface and annihilating in the bulk close to the surface.

When the voltage is applied the bulk director orientation changes to a horizontal orientation and again a loop is formed which, over time, decreases in size until it disappears, leaving the director orientation in the planar state when the voltage is removed.

As the loop decreases in size the loop ends move together in a way similar to that shown in Fig. 6. Measuring the position of the loop ends we can see in Fig. 11(a) that the edges of the loop begin moving together after a few seconds. If we compared this with Fig. 7(a) we see that here the loop disappears much sooner when switched from HAN to planar than planar to HAN.

Figure 11(b) shows that the volume decreases again in a linear fashion but the maximum volume of the loop is much less than that seen in Fig. 7(b). This can be seen in the experimental results comparing Fig. 4 with Fig. 10. Again the experimental results and numerical results for the volume change of the loop are similar. The differences observed could be due to the small changes in the geometrical structure due to manufacturing processes which may initiate defect. The elastic energy shown in Fig. 11(c) reduces as the loop volume decreases and reaches a constant value at the same time as the loop disappears. This then decreases again as the cell relaxes into the stable planar state.

Taking a closer look at the loop disappearance, shown in Fig. 12(a), we can see that before the pulse is applied there is a $\pi-2\alpha$ defect at point P_1 and a $-\pi+2\alpha$ defect at point P_2 due to the sharp corners. After the pulse has been applied and

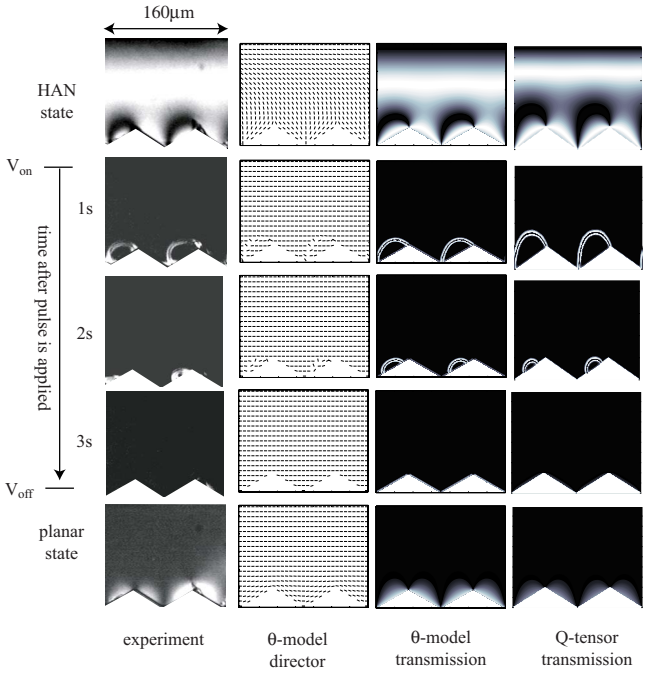

FIG. 10. (Color online) Comparison of experimental results for switching the cell from the HAN state to the planar state with the θ-model director profile, the transmission profile resulting from this director profile and with the Q-tensor model.

the loop ends A and B begin to move together. In Fig. 12(b) we can see that the defect at P_1 has split into a -2α defect, pinned at P_1, and a π defect at point A. Similarly the defect at P_2 has split apart into a 2α defect, pinned at P_2, and a $-\pi$ defect at point B. As time progresses, points A and B come together and annihilate each other, leaving the director profile as shown in Fig. 12(c). This differs from the case when switching from the planar state to the HAN state as in that case there is only one defect moving, from P_2 to P_1.

VI. CONCLUSION

The switching from the planar to the HAN state and also from the HAN to the planar state has been found to be asso-

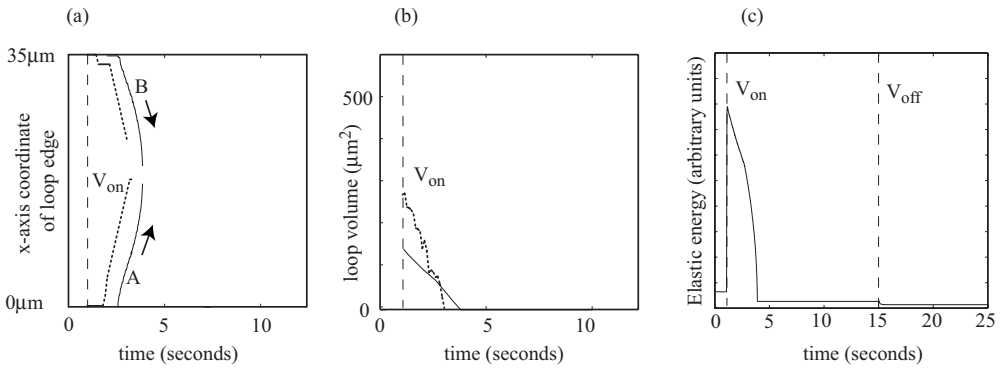

FIG. 11. (a) The x-coordinate of the loop edges versus time as the voltage is applied for experimental data (dashed line) and numerical results (solid line). (b) The volume of the loop decreases in a linear fashion as the voltage is applied for experimental data (dashed line) and numerical results (solid line). (c) The elastic energy of the system also decreases while the voltage is on until it reaches a constant value, then decreases as the cell relaxes into the planar state.

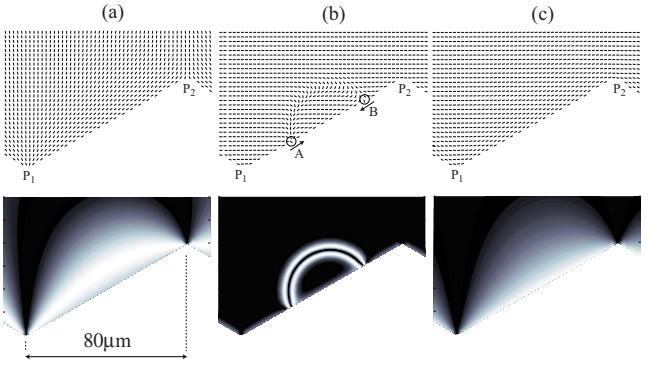

FIG. 12. (Color online) Enlarged plot of the loop annihilation from the HAN state to the planar state. (a) As the voltage is applied the ends of the loops begin to move together along the surface edge. (b) The transmission representation of the director profile in (a).

ciated with the collapsing of filamentlike director reorientation loops (tilt-wall or domain-wall loops) and the associated motion and annihilation of director reorientation points (surface defects) along and close to the edge at the sawtooth sidewall. The predictions from both *n*-director-based Ericksen-Leslie theory and *Q*-tensor theory are in good agreement with the experimental observations of the optical textures between crossed polarizers. The Ericksen-Leslie theory does not describe nematic defect cores because it is restricted to an order parameter of constant magnitude and therefore does not allow the correct representation of defects moving in the bulk of the cell. However, since the defects remain pinned in close vicinity to the sidewall surface this less computationally intensive director-based theory has been found to fully describe the time evolution of the dynamic two-dimensional alignment textures during the switching process as long as finite surface anchoring of the *n*-director is assumed.

These observations can be compared with the switching mechanisms that have been predicted theoretically for flexoelectrically driven switching in similar geometries. References [12,14] consider the zenithal analog of the azimuthal geometry that is reported here and consider a surface relief grating with a sinusoidal or skew-sinusoidal profile. Their predictions are relevant to the current work if any influence of parallel plates that confine the nematic layer into the azimuthal plane is neglected. In Ref. [12], which used a *Q*-tensor theoretical approach, the switching between the two ground states is predicted to occur through the creation and annihilation of pairs of defects. However, in contrast to the observations reported here, the defects move well within the bulk away from the surface during the switching process. In Ref. [14] defect trajectories were investigated using a lattice-Boltzmann scheme during latching between bistable states. It was found that when two defects moved toward each other along the grating surface prior to annihilation their trajectory deviated away from the surface and this deviation was greatest at higher values of the dielectric anisotropy. A submicrometer grating pitch of 0.27 μm was considered and the maximum deviation of the defect trajectory from the grating surface was 0.02 μm. For a grating of pitch 70 μm in the current work this would equate to deviation of 5 μm (making a naive assumption of linear scaling) which would have been observable in our experiments. We would not have been able to detect a deviation of order 2 μm or lower.

In our two-dimensional theoretical analysis the influence of the interactions between the nematic and the parallel plates that confine the nematic layer into the azimuthal plane has been neglected. We obtain good agreement between the observed time evolution of the experimental optical textures and the predictions from the two theoretical approaches using realistic values for the rotational viscosity, elastic constant, and dielectric anisotropy of the nematic material that was used in the investigation. The theoretical predictions shown in Figs. 6(a) and 9(a) for the movement of the surface defects (where the director reorientation loops meet the sidewall surface) are in qualitative agreement with the observed movement but do not reproduce the time dependent velocities of these defects. The surface anchoring at all of the solid surfaces is planar degenerate and evidence that this is weak for azimuthal rotation of the local director comes from the observation that the sidewall morphology is the dominant factor in determining the optical texture [18,20]. This situation obtains for the channel dimensions used in the current study (channel width 90 μm nematic layer thickness 20 μm) but not for nematic layers with a thickness of 10 μm and below where the in-plane switching becomes inhibited.

We have observed asymmetry in the velocities of surface defects having different signs as they move toward each other on the surface prior to annihilation. Defect movement is associated with a dynamic reorientation of the surrounding director field which is in turn coupled to the changing surrounding elastic and velocity flow fields. This has been predicted to lead to defects of opposite strength moving together at different velocities [35–37]. This phenomenon has recently been demonstrated experimentally for $+1/2$ and $-1/2$ defects moving in a nematic layer with very weak azimuthal anchoring at the upper and lower confining plates [38]. In our experimental system the azimuthal anchoring is stronger (a surface anchoring energy of $W=1.75\times10^{-5}$ N m^{-1} was used in the Ericksen-Leslie simulation) and the defects move along a surface rather than freely within the bulk of the nematic layer. The interaction with the surface can interfere with the smooth migration of the defects because temporary pinning can occur at micrometer-scale inhomogeneities on the surface. The properties of the sidewall surface will therefore play a critical role in any azimuthal bistable nematic device where switching involves surface mediated processes.

[1] I. Dozov, M. Nobili, and G. Durand, Appl. Phys. Lett. **70**, 1179 (1997).
[2] R. Barberi, M. Giocondo, and G. Durand, Appl. Phys. Lett. **60**, 1085 (1992).
[3] C. Uche, S. J. Elston, and L. A. Parry-Jones, J. Phys. D **38**, 2283 (2005).
[4] R. N. Thurston, J. Cheng, and G. D. Boyd, IEEE Trans. Electron Devices **27**, 2069 (1980).
[5] G. P. Bryan-Brown, C. V. Brown, and J. C. Jones, UK Patent No. GB2318422 (16 Oct 1995).
[6] G. Barbero, Lett. Nuovo Cimento **29**, 553 (1980).
[7] G. Barbero, Lett. Nuovo Cimento **32**, 60 (1981).
[8] C. V. Brown, V. C. Hui, and G. P. Bryan-Brown, Mol. Cryst. Liq. Cryst. Sci. Technol., Sect. A **301**, 163 (1997).
[9] C. J. P. Newton and T. P. Spiller, in *SID Proceedings of IDRC 97*, edited by J. Morreale (SID, Santa Ana, CA, 1997), p. 13.
[10] C. V. Brown, M. J. Towler, V. C. Hui, and G. P. Bryan-Brown, Liq. Cryst. **27**, 233 (2000).
[11] A. J. Davidson and N. J. Mottram, Phys. Rev. E **65**, 051710 (2002).
[12] L. A. Parry-Jones and S. J. Elston, J. Appl. Phys. **97**, 093515 (2005).
[13] C. Denniston and J. M. Yeomans, Phys. Rev. Lett. **87**, 275505 (2001).
[14] T. J. Spencer and C. M. Care, Phys. Rev. E **74**, 061708 (2006).
[15] G. P. Bryan-Brown, M. J. Towler, M. S. Bancroft, and D. G. McDonnell, UK Patent No. GB2286467 (8 Feb 1995).
[16] S. Kitson and A. Geisow, Appl. Phys. Lett. **80**, 3635 (2002).
[17] N. J. Mottram, A. Ramage, G. Kelly, and A. J. Davidson, UK Patent No. GB20040026582 (8 June 2006).
[18] C. Tsakonas, A. Davidson, C. V. Brown, and N. J. Mottram, Appl. Phys. Lett. **90**, 111913 (2007).
[19] Y. Yi, G. Lombardo, N. Ashby, R. Barberi, J. E. Maclennan, and N. A. Clark, Phys. Rev. E **79**, 041701 (2009).
[20] S. Ladak, A. Davidson, C. V. Brown, and N. J. Mottram, J. Phys. D **42**, 085114 (2009).
[21] C. J. Gerritsma, J. J. M. J. deKlerk, and P. van Zanten, Solid State Commun. **17**, 1077 (1975).
[22] C. Z. van Doorn, J. Appl. Phys. **46**, 3738 (1975).
[23] S. P. Palto and M. I. Barnik, J. Exp. Theor. Phys. **102**, 998 (2006).
[24] N. J. Mottram and C. V. Brown, Phys. Rev. E **74**, 031703 (2006).
[25] I. R. Guralnik, V. N. Belopukhov, G. D. Love, and A. F. Naumov, J. Appl. Phys. **87**, 4069 (2000).
[26] D. Dayton, S. Browne, J. Gonglewski, and S. Restaino, Appl. Opt. **40**, 2345 (2001).
[27] E. B. Priestly, P. J. Wojtowicz, and P. Sheng, *Introduction to Liquid Crystals* (Plenum, New York, 1976).
[28] G. Carbone, G. Lombardo, R. Barberi, I. Musevic, and U. Tkalec, Phys. Rev. Lett. **103**, 167801 (2009).
[29] G. Lombardo, H. Ayeb, and R. Barberi, Phys. Rev. E **77**, 051708 (2008).
[30] I. W. Stewart, *The Static and Dynamic Theory of Liquid Crystals: A Mathematical Introduction* (Taylor & Francis, London, 2004).
[31] P. G. de Gennes and J. Prost, *The Physics of Liquid Crystals*, 2nd ed. (Claridon, Oxford, 1993).
[32] *COMSOL 3.5a*. COMSOL AB, Burlington MA, URL: www.comsol.com, 2007.
[33] A. de Lozar, W. Schopf, I. Rehberg, D. Svensek, and L. Kramer, Phys. Rev. E **72**, 051713 (2005).
[34] M. Born and E. Wolf, *Principles of Optics: Electromagnetic Theory of Propagation, Interface and Diffraction of Light* (Pergamon, New York, 1970).
[35] J. Fukuda, Eur. Phys. J. B **1**, 173 (1998).
[36] G. Tóth, C. Denniston, and J. M. Yeomans, Phys. Rev. Lett. **88**, 105504 (2002).
[37] D. Svensek and S. Zumer, Phys. Rev. E **66**, 021712 (2002).
[38] C. Blanc, D. Svensek, S. Zumer, and M. Nobili, Phys. Rev. Lett. **95**, 097802 (2005).